

## Original research article

## Modified CS-MUSIC for diffuse optical tomography using joint sparsity

B.P.V. Dileep\*, Tapan Das, Pranab K. Dutta

Department of Electrical Engineering, IIT Kharagpur, Kharagpur 721302, India

## ARTICLE INFO

## Article history:

Received 28 November 2017

Accepted 28 December 2017

## Keywords:

Diffuse optical tomography (DOT)

Compressive sensing (CS)

Multiple measurement vector (MMV)

Joint sparsity

Modified CS-MUSIC

## ABSTRACT

In this paper, a modified compressive multiple signal classification (CS-MUSIC) algorithm has been proposed for diffuse optical tomography (DOT) reconstruction. The basic principle involved in DOT is that it illuminates the biological tissue using near infrared light and reconstructs the optical parameters of the tissue from the boundary measurements. The inverse problem of diffuse optical tomography is non-linear and severely ill-conditioned due to the zig-zag nature of light propagation by photons that diffuses through the tissue. Although nonlinear iterative methods are commonly used to solve this problem, they are computationally expensive since the forward problem has to be solved iteratively as well as they do not perform well for complex geometries. Recently, the DOT with compressive sensing (CS) has received a great attention due to its efficient possible reconstructions in DOT imaging. In this, the DOT inverse problem has been formulated as an multiple measurement vector (MMV) problem by using joint sparsity and CS frame work. The modified CS-MUSIC is a novel, non-iterative, and exact algorithm to reconstruct the absorption parameter change for  $\Delta\alpha$  from the boundary data. In addition, this algorithm takes hybridization of sensor array signal processing and probabilistic compressive sensing. The experimental validation of the proposed algorithm has been done on a paraffin wax rectangular phantom through a DOT imaging setup. The performance metrics such as structural similarity index (SSIM), mean square error (MSE), normalized mean square error (NMSE) have been used to evaluate the performance of the reconstruction in this paper. Extensive numerical simulations show that the modified CS-MUSIC algorithm outperforms the current state-of-the-art algorithms and reliably reconstructs the absorption change in DOT.

© 2018 Elsevier GmbH. All rights reserved.

## 1. Introduction

Diffuse optical tomography (DOT) [1] has been considered a promising tool for noninvasive functional imaging of deep biological tissue. In DOT, the tissue is investigated by passing near infrared light (650–950 nm) through the tissue for obtaining the intensity measurements. These boundary measurements have been used to reconstruct the optical properties of interest in DOT. However, the key important aspect of DOT is the reconstruction of optical parameters which come under DOT inverse problem. It is well established from reconstruction methods of DOT that this inverse problem [2] is nonlinear, ill-conditioned and unstable due to the non-linear relation between the optical intensity measurements obtained at the tissue boundary and the optical properties of interest. The predominant effects of biological tissue are optical parameters such

\* Corresponding author.

E-mail addresses: [dileep@iitkgp.ac.in](mailto:dileep@iitkgp.ac.in) (B.P.V. Dileep), [tapandas@iitkgp.ac.in](mailto:tapandas@iitkgp.ac.in) (T. Das), [pkd@ee.iitkgp.ernet.in](mailto:pkd@ee.iitkgp.ernet.in) (P.K. Dutta).

as absorption and scattering coefficients. Imaging the absorption parameter [3] is one of the important consideration in DOT reconstruction since it has been used to diagnose the different states of the biological tissue. While imaging the optical absorption coefficient [4], the scattering coefficient is made constant throughout the volume of the tissue. Generally, the transport of optical photons through a highly scattered medium such as tissue is modeled by using radiative transport equation (RTE) [5]. However, it is computationally very expensive when the complex geometries are considered for DOT imaging. The diffusion equation [6] has played a major role to model the transport of photons through the tissue and it has been derived from RTE. The diffuse optical tomography provides efficient reconstructions in real time applications and hence it has become the important functional imaging tool for biomedical applications. A few applications of the DOT includes breast and brain imaging [7]. There are two different approaches available in conventional DOT reconstruction to deal with the nonlinearity that is inherent in the DOT problem. They are nonlinear iterative and linearization approaches. A few methods that come under nonlinear iterative methods are distorted born [8] and multigrid algorithm [9]. The methods that belong to the linearization approaches are linearized operator method [10] and normalized born method [11]. All these methods fail due to recalculation of the optical flux at each iteration (solving the forward problem) which makes the problem computationally expensive to solve. The technical breakthrough in DOT reconstruction has come from DOT with compressive sensing [12]. The main aim of compressive sensing [13] is to perfectly recover a signal from a few intensity measurements. A few algorithms for solving the MMV problems [16,23] in compressive sensing are simultaneous orthogonal matching pursuit (S-OMP) [14] and  $p$ -thresholding [15]. A novel modified CS-MUSIC algorithm has been proposed in this paper which is non-iterative and exact. This algorithm takes hybridization of sensor array signal processing and probabilistic compressive sensing. In this scenario, the DOT reconstruction problem has been converted to MMV [16,23] problems using the concept of joint sparsity and CS framework. In this modified CS-MUSIC, the first  $k - r$  active indices ( $k$  indicates the sparsity level) are estimated by incorporating the idea from CoSaMP algorithm (compressive sampling matching pursuit) [17] and the remaining  $r$  active coefficients ( $r$  represents dimension of the subspace) are found with a generalized multiple signal classification (MUSIC) algorithm. The proposed algorithm has been validated experimentally on a wax rectangular phantom through a diffuse optical tomography experimental setup. The performance metrics such as structural similarity index (SSIM) [29], mean square error (MSE), normalized mean square error (NMSE) have been used to assess the performance of the DOT reconstruction. It is shown from the numerical simulation results that the proposed algorithm outperforms the conventional MMV algorithms [16,18] like MUSIC, CS-MUSIC, and SA-MUSIC (SA-subspace augmented). The rest of this paper is organized as follows. Mathematical preliminaries are provided in Section 2. The compressive sensing (CS) framework for DOT reconstruction problem is given in Section 3. Section 4 describes the modified CS-MUSIC algorithm. Section 5 demonstrates the experimental studies for DOT reconstruction. The results and discussion are given in Section 6 followed by the conclusion in Section 7.

## 2. Mathematical preliminaries

The mathematical preliminaries for compressive sensing framework for DOT reconstruction problem are provided in this section. The definitions of restricted isometry property (RIP) [19] and mutual coherence [20] has played a major role in applying the concept of CS to the DOT reconstruction problem. The definitions of RIP property and mutual coherence are to be satisfied when the sensing matrix  $A$  must contain the linearly independent columns. Throughout the paper, the  $b$ th row and  $m$ th column of the matrix  $X$  is represented by  $\mathbf{x}^b$  and  $\mathbf{x}_m$  respectively. When the index set is indicated by  $S$ , the corresponding rows of  $X$  is denoted by  $X^S$ , and the columns of  $A$  is given by  $A^S$ .  $\text{supp}X$  indicates the index set which represents the nonzero rows in  $X$ . Note that  $X$  is a matrix for MMV problems.

## 3. Compressive sensing framework for DOT reconstruction problem

We consider the important concept of imaging physics for DOT imaging geometry in DOT reconstruction since it provides convenient measurement detection system using massive detector arrays such as photo detectors. The extension of this theory is applied to time and frequency domain DOT as well. The forward and inverse problem formulations of DOT under MMV will be discussed by using CS framework [21] in detail in this section. The diffusion equation of RTE plays a major role in these MMV based DOT problem formulations.

### 3.1. Formulation of the forward problem using diffusion equation

Considering the turbid medium as highly scattered with very low absorption, the diffusion equation has been considered in continuous wave domain for modeling the light propagation from a continuous wave light source  $q(\mathbf{x}; p)$  for a particular illumination pattern represented by  $p$  [22]

$$\nabla \cdot D(\mathbf{x}) \nabla v(\mathbf{x}, t; p) - \alpha(\mathbf{x}) v(\mathbf{x}, t; p) = -q(\mathbf{x}; p), \quad (1)$$

Here,  $p = 1, 2, \dots, l$ , the absorption and diffusion coefficients are normalized and they are given by  $\alpha(\mathbf{x}) = c\mu_a(\mathbf{x})$  and  $D(\mathbf{x}) = \frac{c}{3(\mu_a(\mathbf{x}) + \mu'_s(\mathbf{x}))}$ , where  $\mu_a(\mathbf{x})$  represents the absorption coefficient,  $\mu'_s(\mathbf{x})$  denotes the reduced scattering coefficient,  $c$  gives the speed of light, and  $\mathbf{x}$  is the location of the target inside the scattered medium respectively. In addition, the optical photon flux

that comes from a continuous wave light source satisfies the given boundary conditions. A form of extrapolated boundary condition has been employed in this MMV based DOT problem formulation and is given by

$$v + \ell \hat{n} \cdot \nabla v = 0 \quad (2)$$

where  $\ell$  indicates the extrapolation length and is calculated by using  $\ell = 2\hat{A}D_0$ ,  $\hat{A}$  denotes the coefficient that depends heavily on the relative refractive index [22],  $D_0$  gives the background diffusion coefficient, and  $\hat{n}$  denotes the direction of normal to the scattered medium. Reconstructing the change in the absorption coefficient  $\Delta\alpha$  is the main target in this paper due to the fact that angiogenesis which are inherent in the cancer disease changes mainly the absorption coefficient of the hemoglobin content and the contrast of this absorption map is very important in DOT imaging. In general, the scattering parameter is much greater than the absorption parameter in the highly turbid medium and accordingly  $\mu_s' \gg \mu_a$ . Hence, the diffusion constant has been made as constant throughout the volume of the tissue such that  $D(\mathbf{x}) = D_0$ . Similarly, we can decompose the absorption parameter as  $\alpha(\mathbf{x}) = \alpha_0 + \Delta\alpha(\mathbf{x})$ , where  $\alpha_0$  indicates the background absorption parameter,  $\Delta\alpha$  provides the change in the absorption parameter. Unlike the conventional DOT imaging methods, we will not assume that the change is much small relative to the background absorption parameter  $\alpha_0$ . The light intensity of scattered flux at position  $\mathbf{x}$  for the  $p$ th specific snapshot is given by the following equation [22]

$$\begin{aligned} \gamma(\mathbf{x}; p) &= \left(1 + \frac{\ell^*}{\ell}\right)^2 [v_0(\mathbf{x}; p) - v(\mathbf{x}; p)], \quad p = 1, 2, \dots, l \\ &= \left(1 + \frac{\ell^*}{\ell}\right)^2 \int g_0(\mathbf{x}, \mathbf{x}') v(\mathbf{x}'; p) \Delta\alpha(\mathbf{x}'; p) d\mathbf{x}' \end{aligned} \quad (3)$$

where  $\ell^* = 3 - \frac{D_0}{c}$ ,  $k_0$  indicates the diffuse wave number and it is calculated by  $k_0 = \sqrt{\frac{\alpha_0}{D_0}}$ . In this DOT reconstruction, we have assumed that the 2D optical coefficients are sparsely distributed at the targets in the turbid medium and can be defined as

$$\Delta\alpha(\mathbf{x}) = \sum_{i=1}^k \Delta\alpha(\mathbf{x}_{(i)}) \delta(\mathbf{x} - \mathbf{x}_{(i)}), \quad \mathbf{x} \in \Omega \quad (4)$$

where  $\delta(\mathbf{x} - \mathbf{x}_{(i)})$  is the delta function, the 2D target locations are denoted by  $\{\mathbf{x}_{(i)}\}_{i=1}^k$  and  $k$  gives the number of optical parameters (targets) and they are unknown in this problem. Here, the assumption is that  $\{\mathbf{x}_{(i)}\}_{i=1}^n$  possible locations of the optical parameters are available on the particular fixed grid, i.e. imaging geometry from which the  $\{\mathbf{x}_{(i)}\}_{i=1}^k$  locations are selected. The scattered flux at the location  $\mathbf{x}$  from the  $p$ th snapshot can be measured by the following equation

$$\beta(\mathbf{x}; p) = \sum_{i=1}^k g_0(\mathbf{x}, \mathbf{x}_{(i)}) v(\mathbf{x}_{(i)}; p) \Delta\alpha(\mathbf{x}_{(i)}), \quad p = 1, 2, \dots, l \quad (5)$$

where  $v(\mathbf{x}; p)$  provides the total incident flux (unknown) that satisfy the Foldy–Lax equation (details are given in Appendix).

### 3.2. MMV based formulations for the DOT inverse problem

This section shows that the DOT imaging problem can be converted to MMV problems [16,23] using the DOT imaging geometry. This geometry for DOT is most commonly used in a large number of the DOT imaging problems. We use different snapshots to image the change in the absorption map accurately for  $\Delta\alpha$ . By collecting the measurement of diffused scattered photon flux (5) at locations of detectors  $\{\mathbf{x}_{d_i}\}_{i=1}^m$ , the DOT inverse problem can be expressed in a matrix form

$$M = AX + B \quad (6)$$

where the scattered flux  $M \in R^{m \times r}$ , and the corresponding noise matrix  $B \in R^{m \times r}$  are computed by

$$\begin{aligned} M &= \begin{pmatrix} \beta(\mathbf{x}_{d_1}; 1) & \dots & \beta(\mathbf{x}_{d_1}; l) \\ \vdots & \ddots & \vdots \\ \beta(\mathbf{x}_{d_m}; 1) & \dots & \beta(\mathbf{x}_{d_m}; l) \end{pmatrix} \\ B &= \begin{pmatrix} b(\mathbf{x}_{d_1}; 1) & \dots & b(\mathbf{x}_{d_1}; l) \\ \vdots & \ddots & \vdots \\ b(\mathbf{x}_{d_m}; 1) & \dots & b(\mathbf{x}_{d_m}; l) \end{pmatrix} \end{aligned} \quad (7)$$

And the sensing matrix  $A \in R^{m \times n}$  is given by

$$A = \begin{pmatrix} g_0(\mathbf{x}_{d_1}; \mathbf{x}_1) & \cdots & g_0(\mathbf{x}_{d_1}; \mathbf{x}_n) \\ \vdots & \ddots & \vdots \\ g_0(\mathbf{x}_{d_m}; \mathbf{x}_1) & \cdots & g_0(\mathbf{x}_{d_m}; \mathbf{x}_n) \end{pmatrix} \quad (8)$$

where the expression for computing  $g_0(\mathbf{x}, \mathbf{x}')$  for a homogeneous scattered medium is written as

$$g_0(\mathbf{x}, \mathbf{x}') = \frac{\exp(-k_0|\mathbf{x} - \mathbf{x}'|)}{4\pi D_0|\mathbf{x} - \mathbf{x}'|} \quad (9)$$

where  $|\mathbf{x} - \mathbf{x}'|$  indicates the distance between  $\mathbf{x}$  and  $\mathbf{x}'$ ,  $\mathbf{x}$  and  $\mathbf{x}'$  are locations of optical coefficients at different points on the geometry of the scattered medium. Here,  $\mathbf{x} = \mathbf{x}_{d_i}$  and  $\mathbf{x}' = \mathbf{x}_i$ . However, 2D greens function of a particular geometry depends on the type of the boundary condition. The right choice of the unperturbed homogeneous 2D greens function will produce the original absorption image with some scaling and few artifacts are always present in it. The illumination dependent induced current matrix  $X$  at targets as in (6) can be expressed as

$$X = \begin{pmatrix} t(\mathbf{x}_1; 1) & \cdots & t(\mathbf{x}_1; l) \\ \vdots & \ddots & \vdots \\ t(\mathbf{x}_n; 1) & \cdots & t(\mathbf{x}_n; l) \end{pmatrix} \quad (10)$$

The rows of  $X$  are nonzero when  $\mathbf{x}_i \in \{\mathbf{x}_{(i)}\}_{i=1}^k$ . Therefore, the sparsity can be expressed as  $k = |X|_0 = \text{supp}X$  (number of targets), where  $|X|_0$  represents the number of nonzero rows (support of  $X$ ) for MMV problems in  $X$ . Moreover, we define the index set of different targets which is indicated by  $C$

$$C = \{j \in \{1, 2, \dots, n\} : \Delta\alpha(\mathbf{x}_{(j)}) \neq 0\} \quad (11)$$

Recall that  $t(\mathbf{x}_j; p) = \nu(\mathbf{x}_j; p)\Delta\alpha(\mathbf{x}_j)$ , where  $\nu(\mathbf{x}_j; p)$  is the photon flux at position  $\mathbf{x}_j$  within the field of view (FOV). Here, our major focus is to reconstruct the optical coefficients of the different targets within the FOV of the scattered medium reachable by the illumination dependent optical current, the photon flux distribution along the paths have been assumed to be a constant value (positive) within the FOV. More clearly,  $t(\mathbf{x}_j; p) = 0$  if  $\Delta\alpha(\mathbf{x}_j) = 0$ . Hence, the sparsity can be defined as  $k = |X|_0 = |C|$ . From the above mentioned equations, the formulation of DOT reconstruction problem can be represented as

$$(Z0) : \min |X|_0 \quad \text{subject to} \quad M = AX + B \quad (12)$$

### 3.3. Exact inversion for absorption change ( $\Delta\alpha$ )

Assume that we have estimated the active index set for the support set of  $C$ , then the corresponding least squares solution  $\hat{X}^C$  depending on  $C$  can be computed by using

$$\hat{X}^C = A_C^\dagger M \quad (13)$$

where the superscript symbol  $\dagger$  represents the pseudo-inverse. Here, the main focus is to estimate the change in the absorption parameter distribution  $\{\Delta\alpha(\mathbf{x}_{(i)})\}_{i=1}^k$  instead of illumination dependent induced current distribution  $\{t(\mathbf{x}_{(i)}; p)\}_{i,p=1}^{k,l}$  (details are given in Appendix). Invoke that for a given estimate  $t(\mathbf{x}_i; p)$ , we can compute the total photon flux  $\nu(\mathbf{x}_i; p)$  with the help of Foldy–Lax equation. Therefore, absorption change ( $\Delta\alpha$ ) can be computed by using least squares technique [24]

$$\Delta\alpha(\mathbf{x}_{(j)}) = \frac{\sum_{p=1}^l (\nu(\mathbf{x}_{(j)}; p))^* t(\mathbf{x}_{(j)}; p)}{\sum_{p=1}^l |\nu(\mathbf{x}_{(j)}; p)|^2}, \quad j = 1, \dots, k, \quad (14)$$

## 4. Modified CS-MUSIC algorithm

All the existing compressive sensing (CS) algorithms to solve the MMV problems in different real applications are based on a probabilistic guarantee but the sensor array signal processing is based on a deterministic guarantee. In order to address the MMV based problems effectively, it is better to consider the best of these two methods which we call hybridization of both methods. In the proposed modified CS-MUSIC algorithm, the first  $k - r$  active indices have been found by incorporating the idea from CoSaMP algorithm (we are not using exact CoSaMP algorithm) and the rest of the  $r$  active indices are estimated with a generalized MUSIC algorithm. While estimating  $k - r$  active indices, we have chosen the sparsity level as  $k - r$  which makes this algorithm to be computationally efficient over the existing algorithms. However, for the case of CS-MUSIC algorithm [16], the first  $k - r$  active indices are estimated by any compressive sensing algorithm such as S-OMP or  $p$ -thresholding and the remaining  $r$  active indices estimated with a generalized MUSIC algorithm. The CS-MUSIC is also called as compressive MUSIC algorithm. The modified CS-MUSIC algorithm is a novel, exact, non-iterative. Also, it takes the hybridization of both



**Fig. 1.** The paraffin wax phantom.

(sensor array processing and compressive sensing). The proposed algorithm can be guaranteed to recover the signal and can be applied to different applications like DOT. The implementation steps of modified CS-MUSIC algorithm are as follows.

1. Estimate signal subspace (dimension of the subspace as  $r$ ) from  $M$  (measurements) using MUSIC algorithm [18].
2. Find  $k - r$  active indices of  $\text{supp}X$  by incorporating the idea from CoSaMP algorithm [17] and we consider the sparsity level as  $k - r$ .
3. Consider  $C_{k-r}$  to be the active indices of  $\text{supp}X$  which are found in step 2 and let  $S = C_{k-r}$ .
4. For each  $f \in \{1, 2, \dots, n\} \setminus C_{k-r}$ , find the parameter set  $\eta(f) = a_f^* [P_{R(Q)} - P_{P_{R(Q)} A_{C_{k-r}}}] a_f$  for each  $f \notin C_{k-r}$ . This step is called generalized MUSIC algorithm [18].
5. For  $f \notin C_{k-r}$ , do the ascending order of  $\eta(f)$  and find the active indices that belongs to the remaining  $r$  elements.

## 5. Experimental studies for DOT reconstruction

The experimental setup and the preparation of wax phantom (rectangular) [25] are described in the experimental studies for DOT reconstruction. The different applications of diffuse optical tomography like breast and brain imaging can be studied using this experimental setup.

### 5.1. Preparation of the paraffin wax phantom

The illustration of paraffin wax phantom is given in Fig. 1. The shape of the wax phantom is in the rectangular with center at (0.25, 0.25) cm (cm indicates centimeter) and having dimensions 0.5 cm  $\times$  0.5 cm has been used in the experimental study. The background material that is considered in the preparation of this phantom are paraffin wax. The paraffin wax is heated first, We have poured the heated solution of wax into the box (rectangular) to form this rectangular phantom. After the heated solution is solidified in the rectangular box, a small hole has been made in it which corresponds to the inclusion within this phantom. The blue ink added to the volume of the hole made on the wax rectangular sample closely mimic like an inclusion having high absorption parameter. The laser source with an optical wavelength of 680 nm has been used in this study. The optical parameter values of paraffin wax are about 0.25 cm<sup>-1</sup> (absorption) and 20 cm<sup>-1</sup> (scattering) respectively and these are measured experimentally.

### 5.2. Experimental setup

The illustration of the experimental setup for diffuse optical tomography is presented in Fig. 2 [25]. The main components (blocks) in the experimental setup are the optical light source, photodetector, and the phantom kept in the rectangular box for study. The semiconductor laser with the operating wavelength of 680 nm and having optical power of 2 mW has been considered as the optical source. The plastic optical fibers of the same size are connected to the optical source for illuminating the rectangular wax phantom at X and Y locations of XY plane in it. The core diameter and length of each plastic optical fiber considered are about 1 mm and 30 cm respectively. The rectangular box consists of holes with spacing almost equal between them at X and Y locations of XY-plane in it. The wax phantom is kept within the rectangular box and the optical fibers of light source and detector have been connected to the holes of the rectangular box to form the source-detector geometry. The collection fiber has been attached to a circular ring held by a strong stand according to their respective position on the boundary surface of the phantom. The photodetector is attached almost close to the collection fiber for measuring the intensity measurements at the sample boundary. The intensity of the light source has been varied so that the intensities at the detector fibers lie within the scale of the photodetector values. The light source is rotated to scan the boundary surface

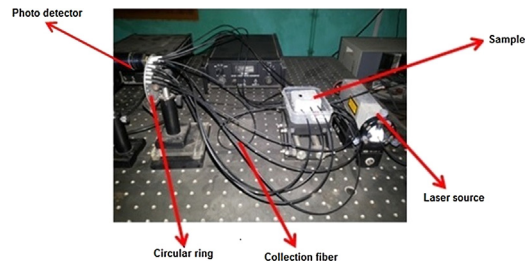


Fig. 2. The experimental setup for DOT.

Table 1

Imaging geometry for DOT with single inclusion.

–	Dt	Sr	Dt	Sr	Dt	–
Dt	Tr*	Tr*	Tr	Tr	Tr	Dt
Sr	Tr*	Tr*	Tr	Tr	Tr	Sr
Dt	Tr	Tr	Tr	Tr	Tr	Dt
Sr	Tr	Tr	Tr	Tr	Tr	Sr
Dt	Tr	Tr	Tr	Tr	Tr	Dt
–	Dt	Sr	Dt	Sr	Dt	–

of the phantom and the intensity measurements are measured by the photodetector. Each time the phantom is translated then rotated manually for changing the source position. For each light source position in the phantom, the photo detector has been moved to each fiber of the collection fiber mounted on a circular ring to collect one measurement reading at a time. The phantom has been translated then rotated eight times which corresponds to eight light source positions in this phantom. We fix the coordinate space of the phantom by this way. In total, three different sets of intensity readings are taken and the average of three sets of readings are considered to be the final intensity measurements at the sample boundary. The entire experiment for DOT is carried out in a dark room environment so we assume the background count as zero. Furthermore, the final intensity measurements at the collection fiber of the sample boundary for the experimental setup considered are affected by various factors like the coupling efficiency of the optical fibers, the light coupling from laser source optical fiber to detector optical fiber via the phantom, and the coupling from a optical source to laser source optical fiber. These factors may vary even though necessary precautions have been taken to keep the position and angle invariant in the boundary surface of phantom. Therefore, calibration of the intensity measurements need to be done by using the whole experimental setup. First, the experiment for DOT is performed with an homogeneous rectangular phantom having absorption parameter values known and the detector measurements at the collection fiber are measured with the help of the photodetector. We define the scale factor for calibration of measurements, and it needs to be changed repeatedly until the simulated measurements is exactly equal to the experimental measurements with required tolerance. Once both the experimental and simulated measurements are almost equal, then we define the corresponding scale factor as the scale factor for the measurements calibration, which tackle the uncertainties carefully that are inherent in the light source and optical detector couplings. The value defined for the scale factor is verified by obtaining both intensity measurements (input and output) by the photodetector. Once the data calibration has done, the optical fibers are kept within the holes and the total experiment for DOT is performed ensuring that the entire experimental setup would not be disturbed. The signal uniformity is achieved at optical fibers (collection fiber) by making the manual adjustment of optical fibers, while the optical source is moved from one optical fiber to another optical fiber such that the total intensity at the fibers is almost the same. The continuous mode of measurement for diffuse optical tomography is used in this study.

## 6. Results and discussion

The illustration of the imaging geometry to simulate the DOT inverse problem for reconstruction of absorption change coefficient is given in this section.

### 6.1. Imaging geometry for simulation of DOT problem

The imaging geometry for simulation of the DOT problem is elaborated in Table 1. The entire geometry has been divided into a number of small grids. The optical sources and detectors are represented by **Sr** and **Dt**. The area inside this geometry will be imaged, i.e., targets within the geometry are denoted by **Tr** and the locations of the inclusion are represented by **Tr\*** respectively. The number of sources and detectors are alternatively connected along the circumference of the boundary of this geometry. In total, 8 sources and 12 detectors are used in this imaging geometry. The optical parameters of the homogeneous background wax phantom are  $0.25 \text{ cm}^{-1}$  (absorption parameter) and  $20 \text{ cm}^{-1}$  (scattering parameter), whereas we consider



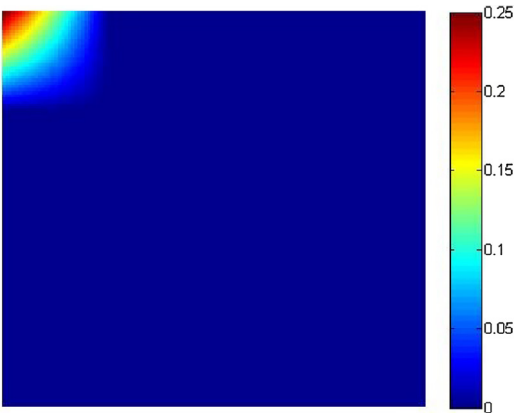


**Fig. 3.** Ground truth map for  $\Delta\mu_a$  ( $\text{cm}^{-1}$ ) for DOT with single inclusion located at top left. (For interpretation of the references to color in this legend, the reader is referred to the web version of the article.)

**Table 2**  
Imaging geometry for DOT with two inclusions.

–	Dt	Sr	Dt	Sr	Dt	–
Dt	Tr*	Tr*	Tr	Tr*	Tr*	Dt
Sr	Tr*	Tr*	Tr	Tr*	Tr*	Sr
Dt	Tr	Tr	Tr	Tr	Tr	Dt
Sr	Tr	Tr	Tr	Tr	Tr	Sr
Dt	Tr	Tr	Tr	Tr	Tr	Dt
–	Dt	Sr	Dt	Sr	Dt	–

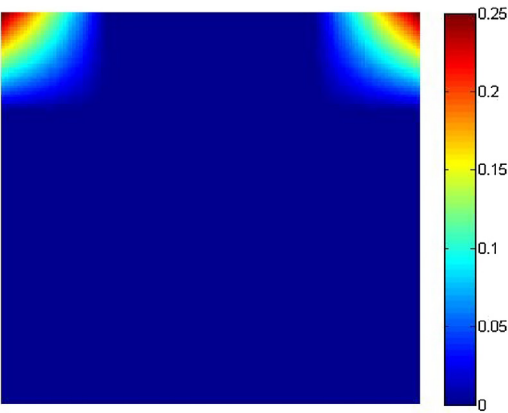


**Fig. 4.** Ground truth map for  $\Delta\mu_a$  ( $\text{cm}^{-1}$ ) for DOT with two inclusions located at top left and right. (For interpretation of the references to color in this legend, the reader is referred to the web version of the article.)

that the maximum change in the absorption parameter for  $\Delta\mu_a$  is  $0.25 \text{ cm}^{-1}$ . The values of  $\Delta\mu_a$  distributed at the imaging targets is known as ground truth values for the change in the absorption parameter as shown in Fig. 3. Since  $\Delta\mu_a$  is sparse at the targets, its minimum value is assumed to be zero at the imaging targets and its maximum value is equal to the background absorption parameter about  $0.25 \text{ cm}^{-1}$  at the location of the inclusion. This ground truth change in the absorption parameter image is taken to be the reference image for  $\Delta\mu_a$  and it can be used further for comparing the reconstructed images of  $\Delta\mu_a$  with it. The red portion in Fig. 3 indicates inclusion. This imaging geometry with single inclusion is considered in this study. The inclusion at the top left corner in Table 1 has center at (0.1, 0.12) cm with the diameter of 0.08 cm.

Imaging geometry for DOT with two inclusions is provided in Table 2. Ground truth map for  $\Delta\mu_a$  ( $\text{cm}^{-1}$ ) (change in the absorption parameter) with two inclusions is presented in Fig. 4. The red portion in Fig. 4 indicates the inclusion. The inclusion at the top left corner in Table 2 has center at (0.1, 0.12) cm and the other inclusion at the top right corner in the same table has center at (0.1, 0.42) cm. Both the inclusions have diameter of 0.08 cm. The simulation is performed using TOAST++ and MATLAB 2013 packages.

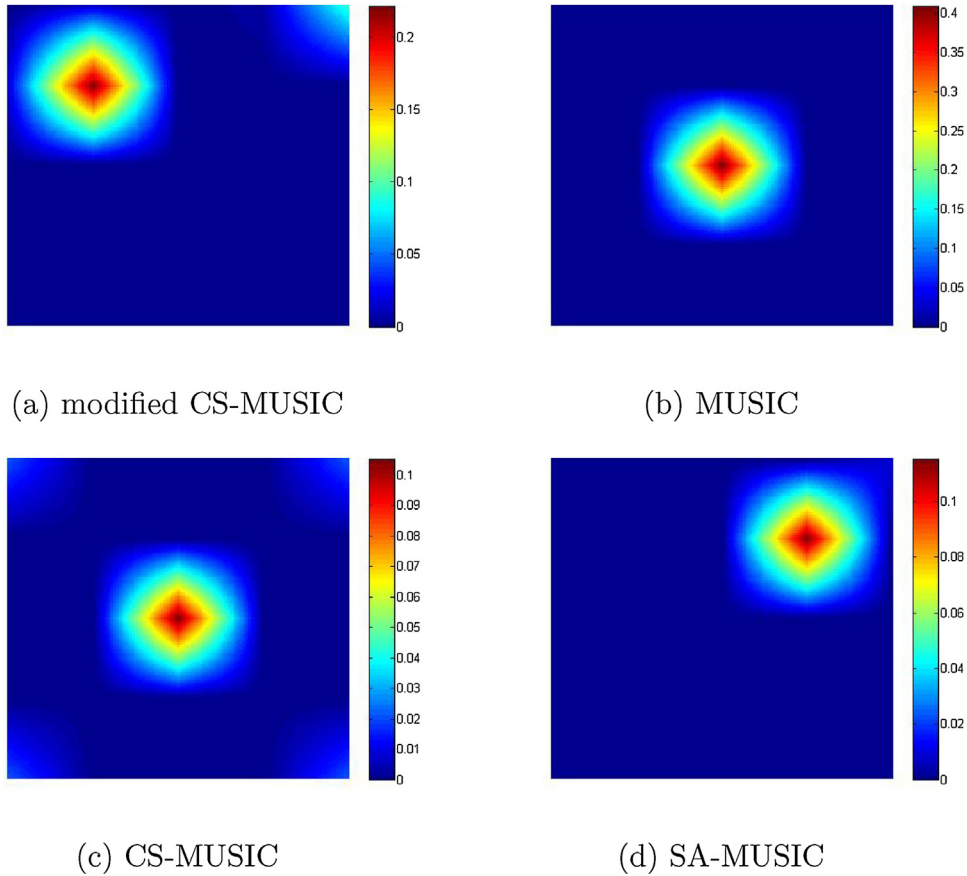


**Fig. 5.** Reconstructed simulated images for  $\Delta\mu_a$  ( $\text{cm}^{-1}$ ) for the case of single inclusion using (a) modified CS-MUSIC, (b) MUSIC, (c) CS-MUSIC, and (d) SA-MUSIC. (For interpretation of the references to color in this legend, the reader is referred to the web version of the article.)

## 6.2. Reconstructed images for $\Delta\mu_a$ (change in the absorption parameter)

By employing the above mentioned imaging geometry's as depicted in Tables 1 and 2, we performed the simulation of DOT reconstruction problem using the proposed algorithm and the given compressive sensing framework and made comparison with the current state-of-the-art algorithms like MUSIC, CS-MUSIC and SA-MUSIC. The reconstructed simulated images for  $\Delta\mu_a$  for both single and two inclusion cases are presented in Figs. 5 and 6. The reconstructed experimental images for  $\Delta\mu_a$  for both single and two inclusion cases are presented in Figs. 7 and 8.

It is noticed from Figs. 5–8 that the reconstructed images for  $\Delta\mu_a$  for the simulated and experimental cases of single and two inclusions appear to be satisfactory. The red portion in Figs. 5–8 represents the inclusion. By comparing Fig. 3 with Figs. 5 and 7, for the case of single inclusion, the modified CS-MUSIC algorithm can identify the location of the inclusion perfectly in the simulated and experimental images and it matches with the ground truth image. The reconstructed value is almost close to the ground truth value. For the MUSIC case, the shift of the location of the inclusion is noticed in the simulated and experimental images and it does not match with the ground truth image, and the reconstructed value does not match with the ground truth value. For the CS-MUSIC and SA-MUSIC case, the shift of the location of the inclusion is observed in the simulated and experimental images and it does not match with the ground truth image. Here also, the reconstructed value does not match with the ground truth value. By comparing Fig. 4 with Figs. 6 and 8, for the case of two inclusions, it was seen that the modified CS-MUSIC algorithm can identify the locations of two inclusions perfectly in both the simulated and experimental images and it matches with the ground truth image, but the reconstructed value is near to the ground truth value. For the MUSIC, CS-MUSIC and SA-MUSIC case, the locations of the two inclusions are not identified correctly in the simulated and experimental images and it does not coincide with the ground truth image. The reconstructed value in these cases also does not match with the ground truth value. Overall modified CS-MUSIC algorithm outperforms other algorithms in identifying both single and two inclusions.



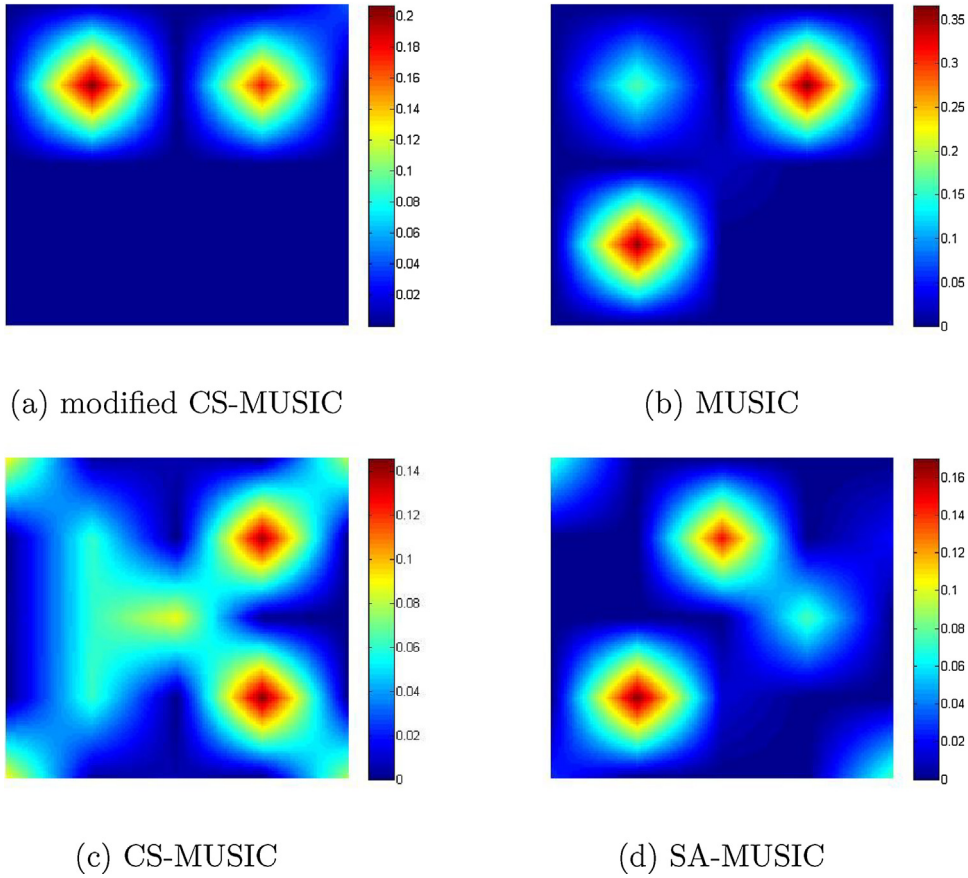


**Fig. 6.** Reconstructed simulated images for  $\Delta\mu_a$  ( $\text{cm}^{-1}$ ) for the case of two inclusions using (a) modified CS-MUSIC, (b) MUSIC, (c) CS-MUSIC, and (d) SA-MUSIC. (For interpretation of the references to color in this legend, the reader is referred to the web version of the article.)

### 6.3. The performance metrics for the evaluation of the reconstructed images

The performance metrics for the evaluation of the reconstructed images for  $\Delta\mu_a$  is presented in this section. Generally, the performance metrics are used to assess the performance of the proposed algorithm in comparison to the current state-of-the-art algorithms in DOT reconstruction. The performance metrics like structural similarity index (SSIM), mean square error (MSE), normalized mean square error (NMSE) are considered in this work which can be computed as follows.

The SSIM is considered to assess the actual similarity between the ground truth absorption change image (original) and the reconstructed absorption change image. For comparison of two such images  $a$  (ground truth map for  $\Delta\mu_a$  depicted in Figs. 3 and 4) and  $b$  (any reconstructed image for  $\Delta\mu_a$  depicted in Figs. 5–8), SSIM can be calculated as

$$S(a, b) = \frac{(2\mu_a\mu_b + c_1)(2\sigma_{ab} + c_2)}{(\mu_a^2 + \mu_b^2 + c_2)(\sigma_a^2 + \sigma_b^2 + c_2)} \quad (15)$$

where  $\mu_a, \mu_b, \sigma_{ab}, \sigma_a$ , and  $\sigma_b$  are the mean, covariance of image  $a$  and  $b$ , and standard deviation respectively. The measured value of SSIM must lie in the range from  $-1$  to  $+1$ . A very high value of SSIM represents that the reconstructed absorption change image for  $\Delta\mu_a$  is much more closer to the ground truth absorption change map of  $\Delta\mu_a$  i.e., the structural distortion (artifacts) in the reconstructed absorption change image is less. Similarly, we can compute the structural dissimilarity by

$$\frac{(1 - S(a, b))}{2} \quad (16)$$

The mean square error (MSE) is computed by

$$\frac{1}{N} \sum_{i=1}^N (\mu_a^r - \mu_a^a)^2 \quad (17)$$

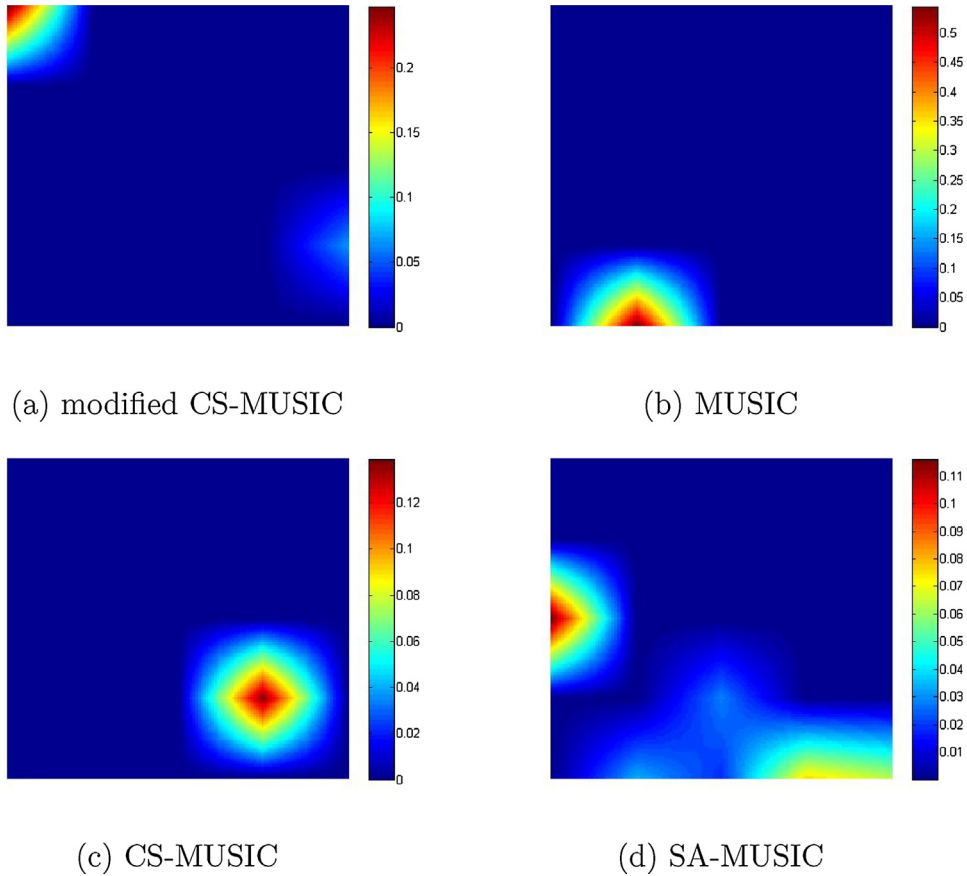


**Fig. 7.** Reconstructed experimental images for  $\Delta\mu_a$  ( $\text{cm}^{-1}$ ) for the case of single inclusion using (a) modified CS-MUSIC, (b) MUSIC, (c) CS-MUSIC, and (d) SA-MUSIC. (For interpretation of the references to color in this legend, the reader is referred to the web version of the article.)

**Table 3**

Performance metrics for the simulated case of single inclusion.

Performance metrics	Modified CS-MUSIC	MUSIC	CS-MUSIC	SA-MUSIC
SSIM	0.8069	0.07	0.3146	0.3611
MSE	0.001	0.0717	0.0029	0.0035
NMSE	0.0540	0.2331	0.1214	0.1370

**Table 4**

Performance metrics for the simulated case of two inclusions.

Performance metrics	modified CS-MUSIC	MUSIC	CS-MUSIC	SA-MUSIC
SSIM	0.5642	0.0086	0.2521	0.1327
MSE	0.0028	0.0548	0.0062	0.0063
NMSE	0.0802	0.1554	0.1512	0.1522

The normalized mean square error (NMSE) is calculated as follows

$$\frac{1}{N} \sum_{i=1}^N \left( \frac{\mu_a^r - \mu_a^a}{\mu_a^a} \right)^2 \quad (18)$$

where  $\mu_a^a$  and  $\mu_a^r$  are the actual and reconstructed absorption parameters,  $N$  denotes the total number of absorption parameters. The performance metrics that are compared for the simulated and experimental cases of single and two inclusions have been provided in Tables 3–6 respectively.

It is evident from Tables 3–6 that the MSE and NMSE (performance metrics) produced by modified CS-MUSIC is significantly less in comparison to the MSE and NMSE produced by other algorithms like MUSIC, CS-MUSIC, and SA-MUSIC. It is also noticed that the SSIM value produced by the modified CS-MUSIC is significant as compared to the SSIM value provided by other algorithms. Hence, the performance metrics for the proposed algorithm (modified CS-MUSIC) is comparatively

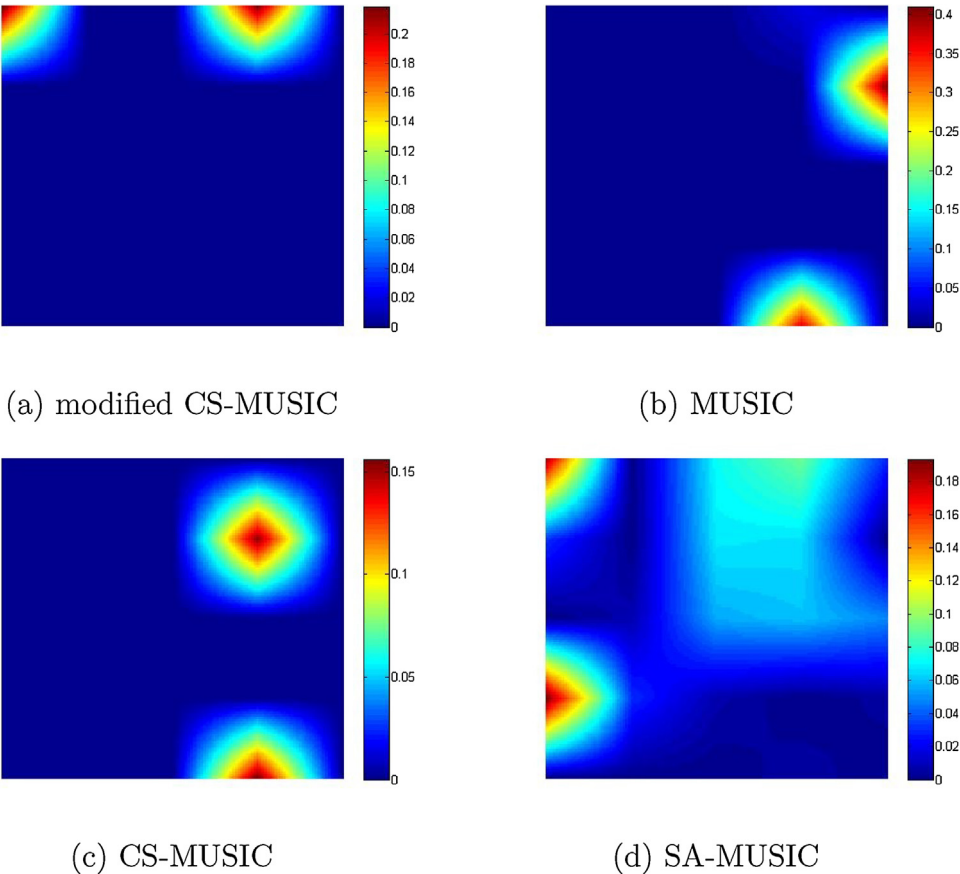


**Fig. 8.** Reconstructed experimental images for  $\Delta\mu_a$  ( $\text{cm}^{-1}$ ) for the case of two inclusions using (a) modified CS-MUSIC, (b) MUSIC, (c) CS-MUSIC, and (d) SA-MUSIC. (For interpretation of the references to color in this legend, the reader is referred to the web version of the article.)

**Table 5**  
Performance metrics for the experimental case of single inclusion.

Performance metrics	modified CS-MUSIC	MUSIC	CS-MUSIC	SA-MUSIC
SSIM	0.8413	0.1010	0.2641	0.1571
MSE	0.0021	0.0938	0.0036	0.006
NMSE	0.0823	0.2799	0.1376	0.1563

**Table 6**  
Performance metrics for the experimental case of two inclusions.

Performance metrics	modified CS-MUSIC	MUSIC	CS-MUSIC	SA-MUSIC
SSIM	0.5593	0.0134	0.0770	0.2806
MSE	0.003	0.0777	0.0067	0.0069
NMSE	0.0969	0.1761	0.1561	0.1575

good as compared to other algorithms which again shows the potential of the proposed algorithm in DOT reconstruction. We can calculate the original absorption parameter for  $\mu_a^r$  by adding the absorption change for  $\Delta\mu_a$  to the background absorption parameter  $\mu_0$ . This avoids the singularity (division by zero) problem in calculating NMSE that are inherent in the DOT reconstruction.

## 7. Conclusion

In this paper, a novel, non-iterative and exact modified CS-MUSIC algorithm has been proposed for diffuse optical tomographic reconstruction. Under the assumption of sparse optical coefficients of inclusion in the investigated sample, the DOT inverse problem has been formulated as an MMV problem using joint sparsity and compressive sensing framework. Numerical simulation results confirm that the proposed algorithm has outperformed other algorithms like MUSIC, CS-MUSIC, and SA-MUSIC. The experimental validation of the proposed algorithm has been done on a wax rectangular sample through an

experimental setup. The performance metrics like SSIM, MSE, and NMSE have been used to assess the performance of the reconstruction in diffuse optical tomography. The reconstruction shows that modified CS-MUSIC based DOT performs better than the other algorithms. The benefit attained from this CS based DOT is that the forward problem need not be solved iteratively which makes the computation time to solve this problem less.

### Foldy–Lax equation

The Foldy–Lax equation [24,26–28] can be computed by

$$v(\mathbf{x}_j; p) = v_0(\mathbf{x}_j; p) + \sum_{i \neq j} g_0(\mathbf{x}_j, \mathbf{x}_i) v(\mathbf{x}_i; p) \times \Delta\alpha(\mathbf{x}_i), \quad (19)$$

where  $p = 1, 2, \dots, l$  and  $i, j = 1, 2, \dots, k$ . In this scenario, we have considered the multiple scattering of optical photons from each of all possible scattered target points except the optical field of self point to avoid the singularity that is inherent in the DOT reconstruction. We can describe the homogeneous 2D green's function  $g_0(\mathbf{x}, \mathbf{x}')$  as

$$(\nabla^2 - k_0^2)g_0(\mathbf{x}, \mathbf{x}') = -\frac{1}{D_0}\delta(\mathbf{x} - \mathbf{x}') \quad (20)$$

And we can compute the homogeneous flux  $v_0(\mathbf{x}; p)$  as

$$v_0(\mathbf{x}; p) = \int g_0(\mathbf{x}, \mathbf{x}') q(\mathbf{x}'; p) d\mathbf{x}', \quad p = 1, 2, \dots, l \quad (21)$$

where  $\mathbf{x} = \mathbf{x}_j$  and  $\mathbf{x}' = \mathbf{x}_i$ .

### The description of $\{t(\mathbf{x}_i; p)\}_{i,p=1}^{k,l}$

Since  $t(\mathbf{x}_j; p) = v(\mathbf{x}_j; p)\Delta\alpha(\mathbf{x}_j)$ , we can write the expanded form of  $\{t(\mathbf{x}_i; p)\}_{i,p=1}^{k,l}$  by the following vector equation

$$\begin{bmatrix} t(\mathbf{x}_i; 1) \\ \vdots \\ t(\mathbf{x}_i; l) \end{bmatrix} = \Delta\alpha(\mathbf{x}_i) \begin{bmatrix} v(\mathbf{x}_i; 1) \\ \vdots \\ v(\mathbf{x}_i; l) \end{bmatrix}, \quad i = 1, \dots, k, \quad (22)$$

### References

- [1] D.A. Boas, D.H. Brooks, E.L. Miller, C.A. DiMarzio, M. Kilmer, R.J. Gaudette, Q. Zhang, Imaging the body with diffuse optical tomography, *IEEE Signal Process. Mag.* 18 (6) (2001) 57–75.
- [2] S.R. Arridge, J.C. Schotland, Optical tomography: forward and inverse problems, *Inverse Probl.* 25 (12) (2009) 123010.
- [3] R.J. Gaudette, D.H. Brooks, C.A. DiMarzio, M.E. Kilmer, E.L. Miller, T. Gaudette, D.A. Boas, A comparison study of linear reconstruction techniques for diffuse optical tomographic imaging of absorption coefficient, *Phys. Med. Biol.* 45 (4) (2000) 1051.
- [4] S.R. Arridge, Optical tomography in medical imaging, *Inverse Probl.* 15 (2) (1999) R41.
- [5] S. Arridge, M. Schweiger, M. Hiraoka, D. Delpy, A finite element approach for modeling photon transport in tissue, *Med. Phys.* 20 (2) (1993) 299–309.
- [6] M. Schweiger, S.R. Arridge, I. Nissilä, Gauss–Newton method for image reconstruction in diffuse optical tomography, *Phys. Med. Biol.* 50 (10) (2005) 2365.
- [7] A. Gibson, J. Hebden, S.R. Arridge, Recent advances in diffuse optical imaging, *Phys. Med. Biol.* 50 (4) (2005) R1.
- [8] Y. Yao, Y. Wang, Y. Pei, W. Zhu, R.L. Barbour, Frequency-domain optical imaging of absorption and scattering distributions by a born iterative method, *JOSA A* 14 (1) (1997) 325–342.
- [9] J.C. Ye, C.A. Bouman, K.J. Webb, R.P. Millane, Nonlinear multigrid algorithms for Bayesian optical diffusion tomography, *IEEE Trans. Image Process.* 10 (6) (2001) 909–922.
- [10] V.A. Markel, V. Mital, J.C. Schotland, Inverse problem in optical diffusion tomography. III. Inversion formulas and singular-value decomposition, *JOSA A* 20 (5) (2003) 890–902.
- [11] V. Ntziachristos, R. Weissleder, Experimental three-dimensional fluorescence reconstruction of diffuse media by use of a normalized born approximation, *Opt. Lett.* 26 (12) (2001) 893–895.
- [12] J. Prakash, C.B. Shaw, R. Manjappa, R. Kanhirodan, P.K. Yalavarthy, Sparse recovery methods hold promise for diffuse optical tomographic image reconstruction, *IEEE J. Sel. Top. Quant. Electron.* 20 (2) (2014) 74–82.
- [13] R.G. Baraniuk, Compressive sensing [lecture notes], *IEEE Signal Process. Mag.* 24 (4) (2007) 118–121.
- [14] J.A. Tropp, A.C. Gilbert, M.J. Strauss, Algorithms for simultaneous sparse approximation: Part I. Greedy pursuit, *Signal Process.* 86 (3) (2006) 572–588.
- [15] R. Gribonval, H. Rauhut, K. Schnass, P. Vandergheynst, Atoms of all channels, unite! Average case analysis of multi-channel sparse recovery using greedy algorithms, *J. Fourier Anal. Appl.* 14 (5) (2008) 655–687.
- [16] J.M. Kim, O.K. Lee, J.C. Ye, Compressive music: revisiting the link between compressive sensing and array signal processing, *IEEE Trans. Inf. Theory* 58 (1) (2012) 278–301.
- [17] J. Tropp, D. Needell, R. Vershynin, Iterative signal recovery from incomplete and inaccurate measurements, *Proc. Information Theory and Applications Workshop* (2008).
- [18] K. Lee, Y. Bresler, M. Junge, Subspace methods for joint sparse recovery, *IEEE Trans. Inf. Theory* 58 (6) (2012) 3613–3641.
- [19] E.J. Candès, J. Romberg, T. Tao, Robust uncertainty principles: exact signal reconstruction from highly incomplete frequency information, *IEEE Trans. Inf. Theory* 52 (2) (2006) 489–509.
- [20] D.L. Donoho, M. Elad, Optimally sparse representation in general (nonorthogonal) dictionaries via  $\ell^1$  minimization, *Proc. Natl. Acad. Sci. U.S.A.* 100 (5) (2003) 2197–2202.

- [21] O. Lee, J.M. Kim, Y. Bresler, J.C. Ye, Compressive diffuse optical tomography: noniterative exact reconstruction using joint sparsity, *IEEE Trans. Med. Imaging* 30 (5) (2011) 1129–1142.
- [22] V.A. Markel, J.C. Schotland, Inverse problem in optical diffusion tomography. II. Role of boundary conditions, *JOSA A* 19 (3) (2002) 558–566.
- [23] J. Chen, X. Huo, Theoretical results on sparse representations of multiple-measurement vectors, *IEEE Trans. Signal Process.* 54 (12) (2006) 4634–4643.
- [24] J.C. Ye, S.Y. Lee, Y. Bresler, Exact reconstruction formula for diffuse optical tomography using simultaneous sparse representation, in: 5th IEEE International Symposium on Biomedical Imaging: From Nano to Macro, ISBI 2008, IEEE, 2008, pp. 1621–1624.
- [25] B. Dileep, T. Das, P.K. Dutta, Greedy algorithms for diffuse optical tomography reconstruction, *Opt. Commun.* 410 (2018) 164–173.
- [26] L. Tsang, J.A. Kong, K.-H. Ding, C.O. Ao, *Scattering of Electromagnetic Waves, Numerical Simulations*, Vol. 25, John Wiley & Sons, 2004.
- [27] M.I. Mishchenko, L.D. Travis, A.A. Lacis, *Multiple Scattering of Light by Particles: Radiative Transfer and Coherent Backscattering*, Cambridge University Press, 2006.
- [28] A.C. Fannjiang, Compressive inverse scattering: I. High-frequency SIMO/MISO and MIMO measurements, *Inverse Probl.* 26 (3) (2010) 035008.
- [29] Z. Wang, A.C. Bovik, H.R. Sheikh, E.P. Simoncelli, Image quality assessment: from error visibility to structural similarity, *IEEE Trans. Image Process.* 13 (4) (2004) 600–612.